

Quantization-induced Control Error in a Digitally Controlled System

Gábor Csernák

Received: date / Accepted: date

Abstract The "noise" induced by quantization in digitally controlled systems can be modelled as small amplitude chaotic behaviour described by a simple piecewise linear map, the micro-chaos map. The chaotic nature of certain micro-chaos maps was proved rigorously in the last 20 years. It was also pointed out that several disconnected strange attractors or repellers may coexist far from the desired state of the system. The control error is influenced by the number of these strange sets and the local behaviour of trajectories in their neighbourhoods. In the present paper we focus on the exploration of the possible attractor/repeller structures in the phase space of a PD-controlled system and estimate the expected control error by several methods.

Keywords digital control · hybrid system · baker's map · Smale horseshoe · micro-chaos

1 Introduction

Quantization and sampling may lead to small-scale chaotic vibrations in digitally controlled systems [1–5]. These vibrations are often neglected or considered as noise in the engineering practice [6]. It was shown in [7] that several small strange attractors can coexist in the phase-space of a simple PD (proportional-differential) controlled linear system. Although the amplitude of chaotic vibrations was found to be indeed small, the large distance of the attracting structures from the desired po-

sition showed that the digital effects can have a significant influence on the control error.

Our goal is the detailed exploration of the phase-space structures of the aforementioned PD controlled oscillator in order to be able to provide reliable estimates for the control error. Section 2 is devoted to the introduction of the mathematical model – basically, it corresponds to a digitally controlled inverted pendulum linearized about the upright (desired) position. In Section 3, the stability properties of the desired position are examined, taking into account the effects of sampling but temporarily disregarding the quantization. As a consequence of the quantization, the phase-space can be divided into parallel bands. These bands play a major role in the dynamics of the system. For example, the number of true fixed points is strongly related to the properties of the bands, as it is described in Section 4. The true fixed points may turn to virtual ones by border collision bifurcations at the borders between the bands, i.e., at the so-called switching lines. Between each pair of true fixed points – and even between a true and a virtual fixed point – strange sets may occur in the neighbourhoods of the switching lines. Section 5 is devoted to the detailed examination of these strange repellers and attractors. Conditions of crisis bifurcations and jump criteria are formulated that can be exploited for the determination of the strange set's attracting/repelling properties. Considering the complexity of the phase-space structure and in search for a method for the reliable estimation of control error in more realistic models, we developed analytical estimation methods for the cases that can be encountered in practice (Section 6). The results are summarized and discussed in Section 7.

Although the considered model seems to describe only the dynamics of the interaction between digital

G. Csernák
MTA-BME Research Group on Dynamics of Machines and Vehicles
Tel.: +36-1-4631227
Fax: +36-1-4633471
E-mail: csernak@mm.bme.hu

computers and the continuous physical world, we hope that our results can be utilized for the analysis of other hybrid systems even in other branches of science (e.g., population dynamics [8] and neurology [9]), too.

2 Mathematical Model

We examine a linear oscillator with an unstable equilibrium at $x = 0$, $\dot{x} = 0$ that is stabilized by a digital control system. To highlight the inherent differences between analogue and digital control systems, we consider the equation of motion of the oscillator under analogue PD control first:

$$M\ddot{x}(t) + c\dot{x}(t) - kx(t) = -\tilde{P}x(t) - \tilde{D}\dot{x}(t). \quad (1)$$

Here $x(t)$ is the coordinate, M denotes mass, $c \geq 0$ is the damping coefficient, while $k > 0$ denotes the stiffness parameter. The proportional gain \tilde{P} and the differential gain \tilde{D} correspond to a virtual spring and a virtual dashpot, respectively.

If digital control is applied, the effects of sampling and quantization must also be taken into account. Sampling means that the information about the state of the system (e.g., displacement and velocity) is periodically refreshed, according to the sampling period τ . We assume that the control force is constant between the successive sampling instants, and its value is immediately available just after sampling, i.e., the processing delay is negligible. Moreover, as a consequence of the quantization, the control force must be an integer multiple of a certain resolution ΔF . Thus, the equation of motion between the j^{th} and $(j+1)^{\text{st}}$ sampling instants can be written as

$$\ddot{x}(t) + \frac{c}{M}\dot{x}(t) - \frac{k}{M}x(t) = -\frac{\Delta F}{M}\text{Int}\left(\frac{\tilde{P}x_j + \tilde{D}\dot{x}_j}{\Delta F}\right), \quad (2)$$

where $t \in [j\tau, (j+1)\tau)$, $x_j \equiv x(j\tau)$ and $\dot{x}_j \equiv \dot{x}(j\tau)$ denote the displacement and velocity at the j^{th} sampling, respectively. The $\text{Int}()$ function rounds towards the origin.

Let us introduce the dimensionless coordinate $y = Mx/(\Delta F\tau^2)$ and the dimensionless time $T = t/\tau$ where τ is the sampling time and t is the physical time. Denoting differentiation with respect to T by prime, the equation of motion turns to

$$y''(T) + 2\beta y'(T) - \alpha^2 y(T) = -\text{Int}(Py_j + Dy'_j), \quad (3)$$

where $T \in [j, (j+1))$ and

$$\begin{aligned} \beta &= \frac{c\tau}{2M}, & \alpha &= \tau\sqrt{\frac{k}{M}}, \\ P &= \frac{\tilde{P}\tau^2}{M}, & D &= \frac{\tilde{D}\tau}{M}. \end{aligned} \quad (4)$$

Parameter α is the ratio of the sampling time and the characteristic time constant of the oscillator. Its value is usually kept very small in practical applications (in the order of $10^{-2} \dots 10^{-5}$) by increasing the sampling frequency.

The general solution of (3) can be determined between the successive sampling instants. As a consequence, one can construct a piecewise linear map $f: \mathbf{y}_j \rightarrow \mathbf{y}_{j+1}$ – referred to as micro-chaos map – in the form

$$\mathbf{y}_{j+1} = \mathbf{U}\mathbf{y}_j + \mathbf{b} \text{Int}(Py_j + Dy'_j) \equiv \mathbf{U}\mathbf{y}_j + \mathbf{b} m_j, \quad (5)$$

where $m_j = \text{Int}(Py_j + Dy'_j)$ and $\mathbf{y}_j = [y_j \ y'_j]^T$. Introducing the notations $\gamma \equiv \sqrt{\alpha^2 + \beta^2}$, $s \equiv \sinh(\gamma)$, $c \equiv \cosh(\gamma)$, and $e \equiv \exp(\beta)$, one obtains

$$\mathbf{U} = \frac{1}{e\gamma} \begin{bmatrix} \gamma c + \beta s & s \\ \alpha^2 s & \gamma c - \beta s \end{bmatrix}, \quad \mathbf{b} = \begin{bmatrix} \frac{e-c}{e\alpha^2} - \frac{\beta s}{e\gamma\alpha^2} \\ -\frac{s}{e\gamma} \end{bmatrix}. \quad (6)$$

The eigenvalues of \mathbf{U} are $\lambda_{1,2}^U = \exp(-\beta \pm \gamma)$. Since $\gamma > \beta$, the state $\mathbf{y} = \mathbf{0}$ is locally unstable and all the other existing fixed or periodic points are saddle points. The corresponding eigenvectors \mathbf{e}_S and \mathbf{e}_U – parallel with the directions of the stable and unstable manifolds of fixed points, respectively – are

$$\mathbf{e}_S = \begin{bmatrix} 1 \\ -\gamma - \beta \end{bmatrix}, \quad \text{and} \quad \mathbf{e}_U = \begin{bmatrix} 1 \\ \gamma - \beta \end{bmatrix}. \quad (7)$$

If the system's state is far from the equilibrium, the quantization (or rounding) of the control force becomes negligible. In this case, the integer part function can be omitted, i.e.,

$$\mathbf{y}_{j+1} \approx \mathbf{U}\mathbf{y}_j + \mathbf{b} (Py_j + Dy'_j) \equiv \mathbf{S}\mathbf{y}_j. \quad (8)$$

$\mathbf{S} = \mathbf{U} + \mathbf{b} \circ [P \ D]^T$, where \circ denotes the dyadic (Kronecker) product and

$$\mathbf{S} = \frac{1}{e\gamma} \begin{bmatrix} \frac{(\alpha^2 - P)(\beta s + \gamma c) + P e \gamma}{\alpha^2} & \frac{\alpha^2 s - (\beta s + \gamma c - e \gamma) D}{\alpha^2} \\ (\alpha^2 - P) s & \gamma c - (\beta + D) s \end{bmatrix}. \quad (9)$$

Let us mention at this point that the micro-chaos map (5) can be rewritten as

$$\mathbf{y}_{j+1} = \mathbf{S}\mathbf{y}_j - \mathbf{b}\chi_j, \quad \text{where } -1 < \chi_j < 1. \quad (10)$$

Thus, the fractional part of the control force is subtracted in this case, instead of the addition of its integer part.

3 Stability of the origin without quantization

The large-scale (macroscopic) behaviour of the system is governed by the matrix \mathbf{S} . Thus, in order to ensure the practical stability [10] of the desired state – which is the usual design goal –, the eigenvalues of matrix

\mathbf{S} must be inside the unit circle in the complex plane. Since stability is a natural requirement for a control system, we restrict ourselves to this case. Note, however, that – since the quantization typically leads to chaotic behaviour – rather long chaotic transients may exist outside the domain of stability, as it was pointed out in [11].

The characteristic equation of matrix \mathbf{S} can be expressed as

$$\mu^2 + \frac{(sD - 2\gamma c)\alpha^2 - P(\gamma(e - c) - \beta s)}{e\gamma\alpha^2}\mu + \frac{\gamma\alpha^2 - Des\alpha^2 - P(e\beta s - e\gamma c + \gamma)}{e^2\gamma\alpha^2} = 0. \quad (11)$$

To check the condition of the asymptotic stability using the Routh-Hurwitz criterions, we introduced a new variable η as $\mu = (\eta + 1)/(\eta - 1)$. It can be shown that $\text{Re}(\eta) < 0 \iff |\mu| < 1$, thus, the characteristic equation can be rewritten as

$$b_2\eta^2 + b_1\eta + b_0 = 0, \quad (12)$$

where

$$\begin{aligned} b_2 &= (P - \alpha^2)\gamma(2ce - 1 - e^2), \\ b_1 &= -\alpha^2(-2sDe + 2\gamma(1 - e^2)) - 2P(ec\gamma - es\beta - \gamma), \\ b_0 &= \alpha^2(\gamma(e^2 + 1 + 2ce) - 2sDe) \\ &\quad - P(2es\beta + \gamma(1 - e^2)). \end{aligned} \quad (13)$$

The origin is asymptotically stable under the application of map $\mathbf{y}_{j+1} = \mathbf{S}\mathbf{y}_j$ if these coefficients are greater than zero. Note that – since $\exp(\beta) > 0$ and $\gamma > 0$ – condition $2ce - 1 - e^2 > 0$ is fulfilled which means that $b_2 > 0$ corresponds to $P > \alpha^2$.

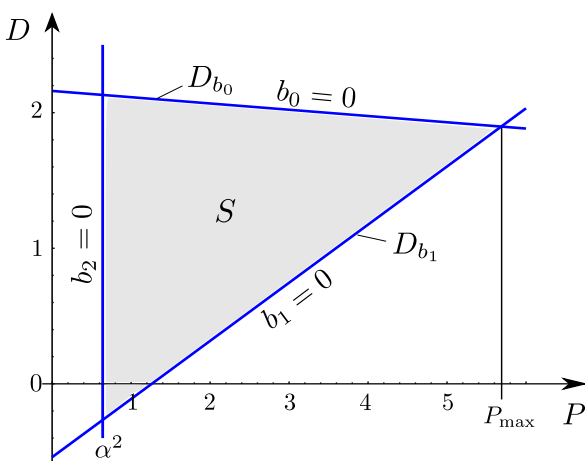


Fig. 1 The domain of asymptotic stability ($|\mu_{1,2}| < 1$) of the desired state $\mathbf{y} = \mathbf{0}$ without considering processing delay and quantization at $\alpha = 0.8$ and $\beta = 0.3$.

The domain of stability of the smooth case (no quantization) is shown in Fig. 1 on the P - D parameter plane

for $\alpha = 0.8$ and $\beta = 0.3$. The differential gain along the curves $b_0 = 0$ and $b_1 = 0$ can be expressed as

$$\begin{aligned} D_{b_0} &= \frac{\alpha^2(1 + 2ce + e^2)\gamma + P((-1 + e^2)\gamma - 2\beta es)}{2\alpha^2 es}, \\ D_{b_1} &= \frac{\alpha^2(\gamma - e^2\gamma) + P((-1 + ce)\gamma - \beta es)}{\alpha^2 es}. \end{aligned} \quad (14)$$

These two lines cross each other at the rightmost corner of the stability domain, at

$$P_{\max} = \frac{\alpha^2(1 - 2ce - 3e^2)}{1 - 2ce + e^2}, \quad (15)$$

$$\begin{aligned} D(P_{\max}) &= \frac{(-3e + 2c^2e + e^3 + c(-1 + e^2))\gamma}{(2ce - e^2 - 1)s} \\ &\quad + \frac{(1 - 2ce - 3e^2)\beta}{(2ce - e^2 - 1)}. \end{aligned} \quad (16)$$

The minimal admissible proportional gain is $P_{\min} = \alpha^2$, according to the condition $b_2 = 0$. In this case, μ_1 or μ_2 becomes 1. At $b_0 = 0$ one of them becomes -1, while at $b_1 = 0$ the characteristic multipliers become complex with unit modulus.

4 Bands, fixed points and periodic orbits

The phase-plane of (5) can be divided into parallel bands, according to the quantization. The control force is the same within such a band, e.g., $m = \text{Int}(Py + Dy')$. The bands are bordered by the switching lines

$$SW_m: \quad y' = \frac{m - Py}{D}, \quad |m| = 1, 2, 3, \dots \quad (17)$$

that cross the horizontal axis at $y = m/P$. The direction field of the mapping and typical example trajectories are shown in Fig. 2.

Since the map (5) is piecewise linear, it can have several equilibria – at most one fixed point in a band. The exact position of the fixed point in the m th band can be given as

$$\mathbf{F}_m \equiv (\mathbf{I} - \mathbf{U})^{-1} \mathbf{b}m = \left[\frac{m}{\alpha^2} \ 0 \right]^T, \quad (18)$$

where \mathbf{I} denotes the unit matrix. To find the fixed point \mathbf{F}_m indeed in band m , the conditions

$$\frac{|m|}{P} \leq \frac{|m|}{\alpha^2} < \frac{|m| + 1}{P} \quad (19)$$

must be fulfilled. If the fixed point \mathbf{F}_m crosses the m th switching line, i.e.,

$$P = \alpha^2 \frac{|m| + 1}{|m|}, \quad (20)$$

a border collision bifurcation occurs and the fixed point becomes virtual. As the instability parameter α is decreased, the border collision bifurcation curves are shifted

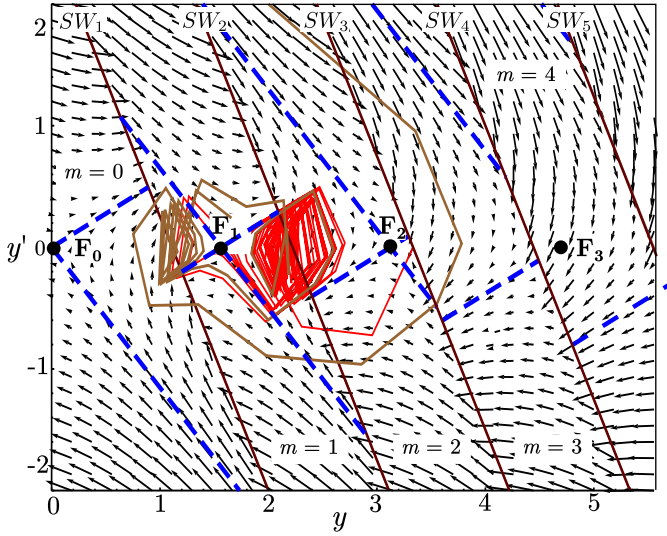


Fig. 2 The direction field of the mapping with switching lines ($SW_1 \dots SW_5$) and fixed points ($F_0 \dots F_3$) with stable and unstable manifolds (dashed lines) at $\alpha = 0.8$, $\beta = 0.3$, $P = 0.9$, and $D = 0.4$. Three true fixed points and one virtual fixed point (F_3) are depicted. Two trajectories are also shown, leading to the same attractor that is a composition of two adjacent repellers. The points of the trajectories are connected with continuous lines for better visualization.

towards smaller values of parameter P . Since the phase-space is symmetric to the origin and the origin is always a true fixed point, the number of true fixed points (see Fig. 3) can be given as

$$N_{\text{fixed}} = 2 \text{Int} \left(\frac{\alpha^2}{P - \alpha^2} \right) + 1. \quad (21)$$

The notions of true and virtual fixed points are illustrated in Fig. 2, where the outmost true fixed point F_2 is in band $m = 2$ and the virtual fixed point F_3 is in band $m = 4$. Even two communicating chaotic repellers are shown in this figure that together form a chaotic attractor. As it will be discussed in the next section, the distribution of disconnected attractors and repellers is closely related to the structure of fixed points. This is why the parameter dependence of the number of true fixed points is important to understand the dynamics of the system.

According to (21), the number of fixed points tends to infinity as $P \rightarrow \alpha^2$, while the origin is the single true fixed point if $P > 2\alpha^2$. Even "supervirtual" fixed points can be born in the latter case by further border collisions of the virtual fixed point at values $P = n\alpha^2$, $n = 2, 3, \dots$

Although parameters D and β do not appear in (21), they influence the size of the domain of stability, i.e., the maximal possible value of the gain P . The minimal possible number of fixed points at a given α, β pair – if P is chosen from the domain of stability – can be found

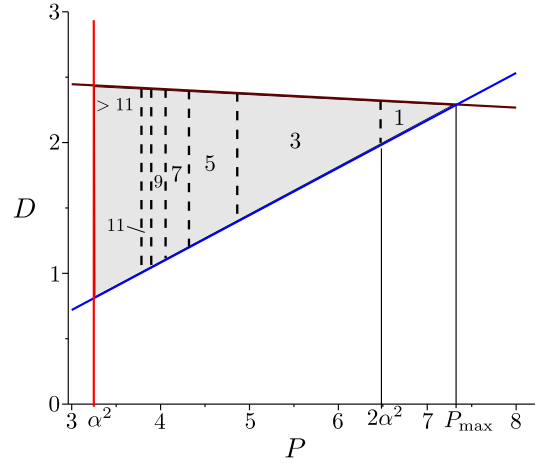


Fig. 3 The number of fixed points at $\alpha = 1.8$ and $\beta = 0.3$ and the border collision bifurcation curves (vertical dashed lines).

by substituting $P = P_{\text{max}}$ to (21). The results are depicted in Fig. 4. In practical applications, the damping

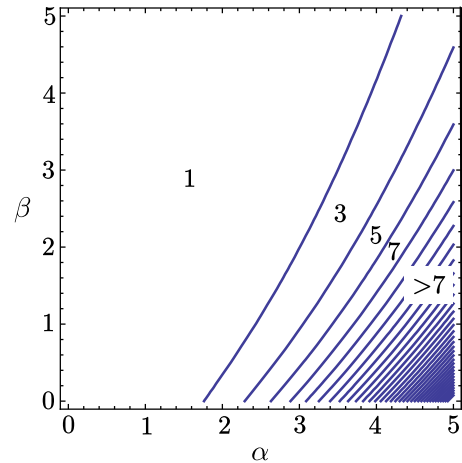


Fig. 4 The minimal number of fixed points if the gains P and D are chosen from the domain of stability. The maximal possible number of fixed points is unbounded.

parameter β is usually small – significantly less than α . Thus, at relatively large values of α ($\alpha \gtrsim 2$), the phase-space structure becomes rather complicated with several fixed points. On the other hand, if α is sufficiently small, e.g., $3\alpha^2 < P$, the supervirtual fixed points – situated several bands away from the true fixed points – can influence the dynamics in the neighbourhood of the origin. The unstable manifold sections of (super)virtual fixed points lead to larger speed values than the manifolds of true fixed points. As a consequence, the corresponding strange sets can also be larger. See Fig. 2, where the diameter of the repeller between F_1 and F_2

is larger than the diameter of the repeller between \mathbf{F}_0 and \mathbf{F}_1 . The manifold sections of (super)virtual fixed points "open up" similarly.

5 Attractors and repellers

5.1 Strange structures between fixed points

As it was shown in [7], strange sets appear in the neighbourhoods of the switching lines between any two true fixed points and even between a true and a virtual fixed point. This property is related to the fact that the control force is quantized. The control force is in equilibrium with other forces at the fixed points. In the simplest case, if a phase-space point is farther away from the origin than the fixed point (i.e., larger control force would be necessary), but in the same band (i.e., the control force is the same), the dynamics will push the trajectory even farther, to the next band. Since the control force is one unit larger there, the dynamics will lead back to the band that is closer to the origin. The evolving structures may be chaotic attractors or repellers with transient chaotic dynamics. According to the reasoning above, the attractor/repeller points between the fixed points \mathbf{F}_{m-1} and \mathbf{F}_m are densely distributed in the neighbourhoods of the crossings of the switching lines and the $y' = 0$ line, i.e., at

$$y_m = \frac{m}{P}. \quad (22)$$

Thus, the strange sets can be indexed by the corresponding integer indices m of switching lines. The attractor in Fig. 2 is a composition of two repellers at the switching lines SW_1 and SW_2 , while there is another repeller at SW_3 with very large escape rate, thus, this latter object is practically undetectable. According to our results, there are parameter domains where several disconnected chaotic attractors coexist in the phase space. Although the diameter of these sets is usually negligibly small in practice, they can reside very far from the origin, leading to remarkable deviance from the desired state.

Since there is a possible attractor or repeller between the "last" true fixed point and the "first" virtual fixed point, the index m_{\max} of the strange structure that is farthest from the origin (cf. (21)) is

$$m_{\max} = \text{Int} \left(\frac{P}{P - \alpha^2} \right). \quad (23)$$

As it will be shown in Section 5.2, the attractors can undergo crisis bifurcations, turning to repellers with transient chaotic behaviour. The escaping trajectories eventually tend to another chaotic attractor or another repeller – that possibly sends back the trajectories. In

the latter case, the two repellers merge, forming a larger attractor. It may also happen – especially at low values of α and high values of parameter P , due to the existence of supervirtual fixed points – that the single attractor at the origin blows up and its diameter becomes several times larger than the distance between the switching lines. The size of the single attractor or the distance of the farthest attractor from the origin provide estimates for the maximal possible control error. To be able to provide reliable estimates, the topology and the global dynamics of the phase-space must be examined in more detail.

5.2 Boundary crisis bifurcations

It was shown in [7] that the phase-space structure can be described as a series of baker's maps. To be able to refine the concepts outlined in [7], we reiterate the notations introduced there. Consider the neighbourhood of the switching line SW_m ($m > 0$) that is between the fixed points \mathbf{F}_l on the left and \mathbf{F}_r on the right. The indices of the corresponding bands are $l = m - 1$ and $r = m$, respectively. The stable and unstable manifolds W_L^S, W_L^U, W_R^S and W_R^U of the two fixed points – where the subscript refers to the fixed point and the superscript refers to the type of the manifold – form a parallelogram, as depicted in Fig. 5. Due to the symmetry of the system, the structure is similar on the negative half-plane. Thus, it is enough to consider here the case $m > 0$.

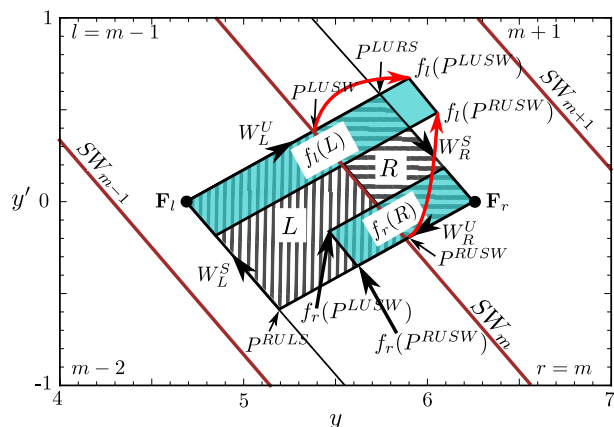


Fig. 5 The phase-space structure between two fixed points.

The parallelogram is divided into two quadrangles L and R by the switching line SW_m . The vertices of the left quadrangle are the fixed point \mathbf{F}_l , the intersection point P^{RULS} of the manifolds W_R^U and W_L^S , the

intersection point P^{RUSW} of W_R^U and the switching line and the crossing point P^{LUSW} of manifold W_L^U and the switching line, see Fig. 5. The vertices of the right quadrangle can be denoted similarly, as shown in the figure. The coordinates of the aforementioned points can be obtained by straightforward analytical calculation:

$$\begin{aligned} P^{LURS} &= \left(\frac{\beta + (2m-1)\gamma}{2\alpha^2\gamma}, \frac{1}{2\gamma} \right), \\ P^{RULS} &= \left(\frac{-\beta + (2m-1)\gamma}{2\alpha^2\gamma}, -\frac{1}{2\gamma} \right), \end{aligned} \quad (24)$$

$$\begin{aligned} P^{RUSW} &= \left(\frac{(\alpha^2 + D(-\beta + \gamma))m}{\alpha^2(-\beta D + D\gamma + P)}, \right. \\ &\quad \left. - \frac{(\beta - \gamma)m(\alpha^2 - P)}{\alpha^2(-\beta D + D\gamma + P)} \right), \\ P^{LUSW} &= \left(\frac{D(\beta - \gamma)(-1 + m) - \alpha^2 m}{\alpha^2(\beta D - D\gamma - P)}, \right. \\ &\quad \left. \frac{(\beta - \gamma)(\alpha^2 m + P - mP)}{\alpha^2(\beta D - D\gamma - P)} \right). \end{aligned} \quad (25)$$

The structure of successive attractors and repellers can be explored based on the properties of the images of the quadrangles L and R . The image of L can be calculated by restricting the dynamics to the band of the fixed point \mathbf{F}_l , i.e., to the case $l = m - 1$. Thus, we can introduce the restricted versions of the micro-chaos map (5): $f_l \equiv f|_{l=m-1}$ and $f_r \equiv f|_{r=m}$. The images of the quadrangles ($f_r(R)$ and $f_l(L)$) are stretched along the unstable manifolds. As it was shown in [7], the four possible pre-images are stretched along the stable manifolds, leading to a horseshoe structure indicating chaotic dynamics.

The images of points P^{LUSW} and P^{RUSW} characterize the stretching of the domains L and R along the unstable directions. On one hand, if $f_l(P^{LUSW})$ or $f_l(P^{RUSW})$ cross the stable manifold W_R^S of \mathbf{F}_r , a boundary crisis bifurcation occurs and trajectories escape from the quadrangle $L \cup R$ away from the origin. This situation is shown in Fig. 5. On the other hand, if $f_r(P^{LUSW})$ or $f_r(P^{RUSW})$ cross the stable manifold W_L^S of \mathbf{F}_l , trajectories escape towards the origin.

The attracting and repelling properties of the phase-space objects between the fixed points can be determined by evaluating the positions of the aforementioned image points. Note, however, that as parameters are changed, point P^{LURS} can be shifted to band $r = m$ or point P^{RULS} to band $l = m - 1$, distorting the results (cf. Fig. 5). This phenomenon is also a special bifurcation whose conditions can be checked easily – typically, the corner points tend to be in a “wrong” band if parameter P is large.

Fig. 6 shows how the attracting/repelling properties of structures at the switching lines vary as the proportional gain is changed. The continuous curves

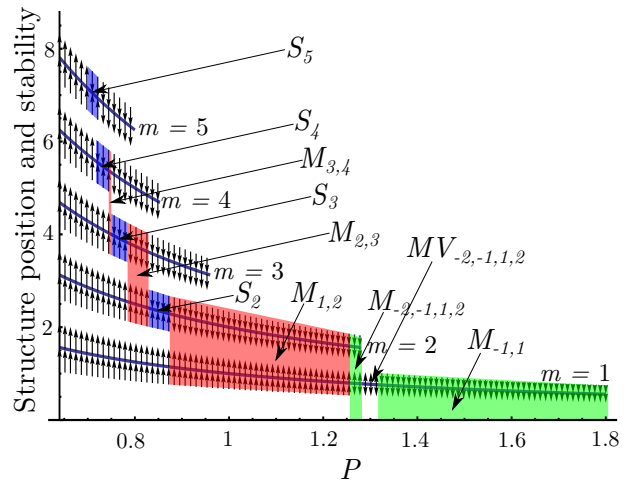


Fig. 6 The attracting/repelling properties of phase-space structures at $\alpha = 0.8$, $\beta = 0.3$ and $D = 0.6$. Shading indicates various attractors.

show the attractor/repeller positions at several values of index m , according to (22). Possible attractors disappear at the border collision bifurcations (20), i.e., at $P = m\alpha^2/(m-1)$, this is why curves with higher index m are shorter. Arrows above the curves indicate the attracting or repelling property of the corresponding structure in the direction away from the origin, while arrows below the curves show these properties in the direction towards the origin. Based on these properties, various types of attractors can be defined. An attractor that is confined to the neighbourhood of the switching line SW_m – i.e., no escape is possible in either direction – is denoted by S_m . If two or more adjacent repellers merge, e.g., that reside in the neighbourhoods of switching lines $m-1$, m and $m+1$, the corresponding large attractor is denoted by $M_{m-1,m,m+1}$. The aforementioned attractors are designated by shaded areas in Fig. 6. Note, that a special attractor exists at $P \approx 1.3$, denoted by $MV_{-2,-1,1,2}$. At these parameters, the first virtual fixed point is \mathbf{F}_1 , thus, no strange set is expected in the position indexed by $m = 2$. Although there is a repeller at SW_1 , the global dynamics leads back towards the origin, resulting in a larger attractor.

It can be shown by differentiation with respect to P that if the parameters are chosen from the domain of stability, the increase of parameter P increases the attractivity of the origin. This trivial result implies that as P is increased, the arrows can flip downwards, only (cf. Fig. 6). Consequently, there are only two different scenarios possible at a certain value of m : both arrows

are directed upwards at small P . As P is increased, either the lower or the upper arrow flips downward. If the upper arrow flips first, a single attractor is born. However, if the lower arrow flips, the structure will repel in both directions. Finally, at even larger values of the proportional gain, the other arrow flips, too, giving rise to a repeller directing the trajectories towards the origin. One can also show analytically that no escape away from the origin is possible close to the border collision bifurcation points, i.e., at the right endpoints of the lines the upper arrows always point downwards.

Four conditions must be checked to decide the directions of both the upper and lower arrows, corresponding to the possible crossings of points with the stable manifolds – i.e., to crisis bifurcations. As follows, the crossing of $f_l(P^{LUSW})$ and $f_l(P^{RUSW})$ with W_R^S will be denoted by $Out+$ and $Out-$, while the crossing of $f_r(P^{RUSW})$ and $f_r(P^{LUSW})$ with W_L^S will be denoted by $In+$ and $In-$, respectively. These four families of crisis bifurcation curves at various values of index m form straight lines on the PD parameter plane, as illustrated in Fig. 7. The corresponding formulae can be derived in a straightforward way.

$Out+$:

$$D = -\frac{\beta e + \gamma(e + 2(c + s)(m - 1))}{\alpha^2 e} P + \frac{2\gamma m(c + s)}{e}. \quad (26)$$

$In+$:

$$D = -\frac{(\beta + \gamma)e - 2\exp(\gamma)\gamma}{\alpha^2 e} P - \frac{2\gamma m \exp(\gamma)}{e}. \quad (27)$$

$Out-$:

$$D = \frac{\gamma((c - e)(\beta + \gamma) - 2c\gamma m)}{(\beta - \gamma)(\alpha^2 s + (\beta + \gamma)(c\gamma - e\gamma + \beta s))} P + \frac{(\alpha^2 + \beta(\beta + \gamma) - 2\gamma^2 m)s}{(\beta - \gamma)(\alpha^2 s + (\beta + \gamma)(c\gamma - e\gamma + \beta s))} P + \frac{2m\alpha^2(c + s)\gamma^2}{(\beta - \gamma)(\alpha^2 s + (\beta + \gamma)(c\gamma - e\gamma + \beta s))}. \quad (28)$$

$In-$:

$$D = \frac{\gamma^2(s + c)(2m - 1) - \gamma^2 e + \beta\gamma(c - e + s)}{(\beta - \gamma)(\alpha^2 s + (\beta + \gamma)(c\gamma - e\gamma + \beta s))} P - \frac{2m\alpha^2(c + s)\gamma^2}{(\beta - \gamma)(\alpha^2 s + (\beta + \gamma)(c\gamma - e\gamma + \beta s))}. \quad (29)$$

The validity of our concept was checked by numerical simulation at equally spaced values of parameters P and D in the domain of stability, omitting the transients. The results are also depicted in Fig. 7. The crosses and plus signs show parameter values where the simulation did not agree with the predicted structure. Crosses (mainly on the left hand side of the figure) mean that not all the predicted bands were visited by the numerical trajectory. Plus signs (at the top and bottom) correspond to parameters where additional bands were visited.

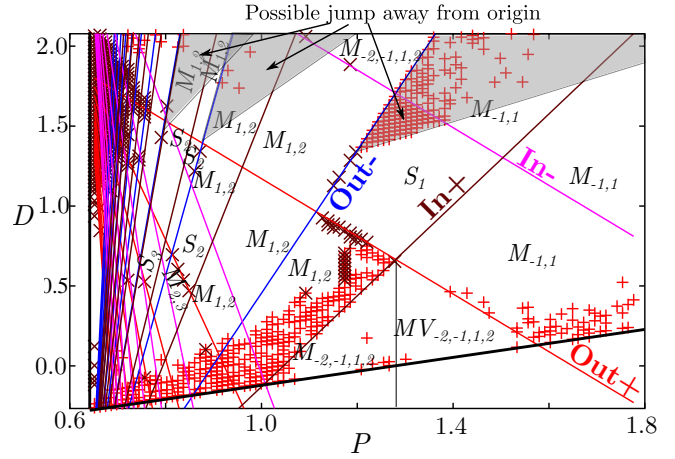


Fig. 7 The types of possible attractors at $\alpha = 0.8$, $\beta = 0.3$ in a part of the domain of stability. Borders of the stable domain: thick solid lines, thin lines: crisis bifurcation curves. S_i denotes domains where a separated attractor exists close to the switching line SW_i . $M_{i,\dots,k}$ denotes domains where a large attractor is formed of merged repellers about the switching lines SW_i, \dots, SW_k . Plus signs: escape. Crosses: not all bands are visited. Outward jumps can occur in the shaded domains.

As it can be seen, there are parameter domains that are evenly covered by plus signs or crosses. The deviance from the expected behaviour is likely to be related to other types of bifurcations in these domains, for example, jumps of the trajectory over whole bands or border collisions of higher-order periodic orbits. The points are scattered in some other parts of the figure. A possible explanation of this fact is that merged attractors are formed by two or more repellers. The number of steps that is necessary to escape from these structures depends both on the parameters and the initial conditions. The dependence on initial conditions is non-smooth, because the basin boundaries are fractals [12]. Thus, the escape time can be very long, this is why the escape was not detected at certain parameters.

5.3 Jumps

There are two kinds of jumps possible: by outward jump we mean that the point $f_l(P^{LUSW})$ or $f_l(P^{RUSW})$ (see Fig. 5) arrives at band $m + n$, $n > 0$ instead of band m . Similarly, inward jump means that $f_r(P^{LUSW})$ or $f_r(P^{RUSW})$ arrives at band $m - 1 - n$, $n > 0$ instead of band $m - 1$. According to the notations of Fig. 5, $l = m - 1$ and $r = m$ are the indices of the fixed points on either side the switching line SW_m . Just as in the previous section, four conditions must be checked at a given parameter set. The bifurcations, corresponding to jumps, occur as the aforementioned image points cross

the switching lines SW_{m+n} or SW_{m-1-n} . Thus, the bifurcation curves can be determined in a straightforward way. Consider first the case of outward jumps.

5.3.1 Outward jumps

The jump of $f_l(P^{LUSW})$ over n bands occurs if

$$(1-m)P(c-e+s) + \alpha^2(cm - e(m+n) + ms) > 0. \quad (30)$$

Since $c - e + s > 0$, the coefficient of P is negative for $m > 1$, thus, small P , large α and small β is necessary to have jumps and this condition is independent of parameter D :

$$P < \alpha^2 \frac{cm - e(m+n) + ms}{(m-1)(c-e+s)}. \quad (31)$$

Moreover, (30) is independent of both P and D at $m = 1$ i.e., when the dynamics in the $m = 0$ (uncontrolled) band governs the jump. Two kinds of jumps are illustrated in Fig. 8, showing a case when it is not enough to examine jumps from the outmost true fixed point for the estimation of the largest control error. The "length" n of possible jumps is approximately proportional with $e^{\gamma-\beta}$, thus, the damping coefficient β has an important effect on this type of outward jumps.

The jump of $f_l(P^{RUSW})$ occurs if

$$P < -\alpha^2 \frac{Ds + \gamma(cm - e(m+n) + ms)}{\beta s - \gamma((c-e)(m-1) + ms)}. \quad (32)$$

The parameter domains where $n = 1 \dots 4$ outward jumps can occur from the neighbourhood of the last true fixed point, i.e., from $m = \text{Int}\left(\frac{P}{P-\alpha^2}\right)$ are shown in Fig. 9. Since small damping is typical in reality, the case $\beta = 0.1\alpha$ is depicted. $\beta = 0$ leads to only slightly different results.

It is worth to note that at small values of α only the D -dependent (cf. (32)) type of outward jumps can occur. Rather counterintuitively, the parameter domain of possible outward jumps *increases* as D is increased. It can be seen in Fig. 7 that the deviation between the simulation and the theoretical prediction can be explained by outward jumps in certain parameter domains – at high values of D . Since the points indicating deviation from the theory are rather scattered, conditions (31) and (32) only open the possibility of outward jumps from strange sets.

5.3.2 Inward jumps

The jump of $f_r(P^{RUSW})$ can occur if

$$P > \alpha^2 \left(1 + \frac{n}{m(e^{\gamma-\beta} - 1)}\right). \quad (33)$$

Just as in the case of condition (30), the length n of jumps is proportional with $e^{\gamma-\beta}$.

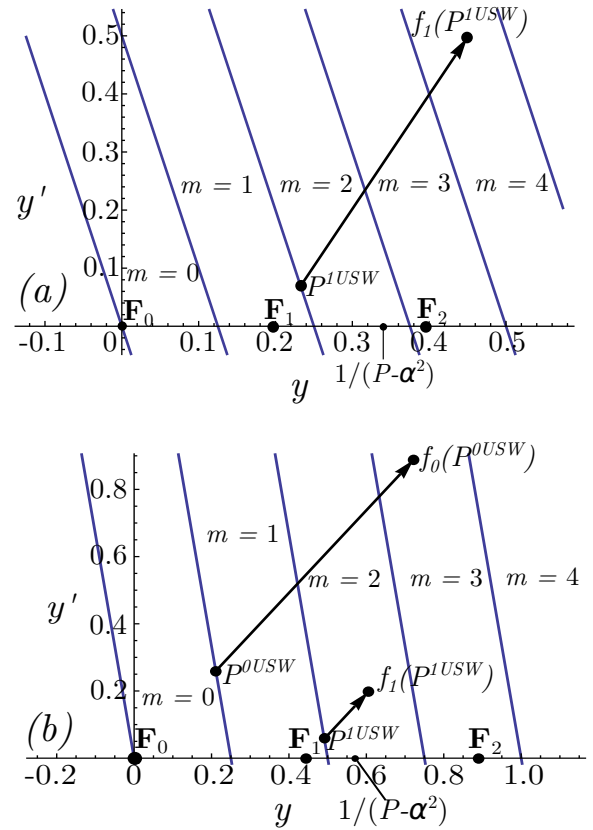


Fig. 8 (a) An outward jump over two whole bands from the outmost true fixed point \mathbf{F}_1 , at $\alpha = 2.25$, $\beta = 0.3$, $P = 8$ and $D = 2$. (b) An example when a large jump occurs from a non-outmost fixed point at $\alpha = 1.5$, $\beta = 0.3$, $P = 4$ and $D = 0.6$.

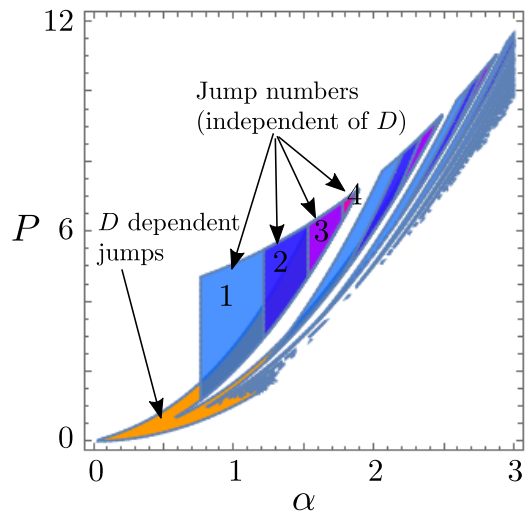


Fig. 9 Parameter domains where jumps $n = 1, 2, 3, 4$ can occur from the last true fixed point, further away from the origin, at $\beta = 0.1\alpha$ and $D = 2$.

The condition of the jump of $f_r(P^{LUSW})$ can be formulated as

$$D > \gamma \frac{(c+s)m + e(n-m)}{s} - \frac{(c-e)\gamma m + (\beta + \gamma(m-1))s}{\alpha^2 s} P. \quad (34)$$

The results are shown in Fig. 10 for the case $m = 1$ and various values of n . We found that the differential gain D has negligible influence on the inward jumps, while the role of parameter β is significant. Since the width of

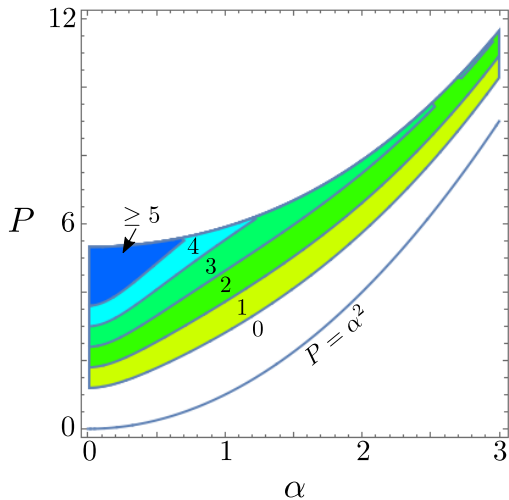


Fig. 10 Parameter domains where inward jumps $n = 1, 2, 3, \dots$ can occur from the switching line at $m = 1$ towards the origin (and to the other half plane), at $\beta = 0.3$ and $D = 2$.

band 0 is twice as much as the widths of other bands, the domain of 1 jump was calculated with substituting $n = 2$ into (33) and (34). One can see that at small values of α and large values of P very large inward jumps may occur. Actually, it means that the trajectory jumps to the other half plane, over several bands. In practical applications this inward jump may contribute a lot to the increase of the control error. To check our results, we took into account

- the outward jumps,
- inward jumps when at least one band was jumped over, and
- inward jumps with $n = 2m + 1$, i.e., when the jump led to the other half-plane, farther from the origin than the initial point.

The results are shown in Fig. 11 at $\alpha = 0.8$ and $\beta = 0.3$. It can be seen that not all the deviances can be explained by the occurrence of jumps, but most of them are related to them.

Certainly, several other mechanisms can also lead to the escape of trajectories from the predicted bands.

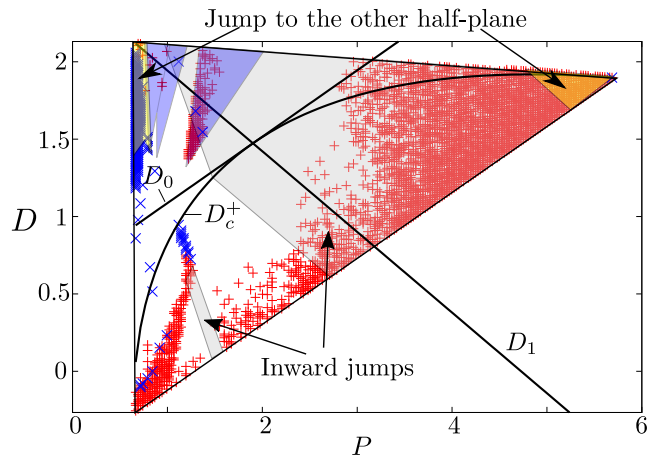


Fig. 11 The whole domain of stability at $\alpha = 0.8$ and $\beta = 0.3$. Parameter domains of possible jumps are shaded. The domains of outward jumps are the three darkest triangles (cf. Fig. 7). Plus signs denote deviances from the theoretical prediction based on crisis bifurcations. The solid curves D_0 , D_1 and D_c^+ divide the stable domain into smaller parts, based on the properties of the eigenvalues of matrix \mathbf{S} .

Unfortunately, the proper description of these mechanisms (e.g. effects of supervirtual fixed points, dynamics along the stable manifold of a virtual fixed point, etc.) is rather complex. Thus, instead of their examination, we developed more general concepts for the estimation of the control error.

Either single or merged attractors exist in the phase-space, they must reside in a finite domain, in a so-called absorbing sphere. The maximal possible control error is related to the diameter of the absorbing sphere. As we saw in this section, the worst scenario occurs when inward jumps can push the trajectories from the positive to the negative half-plane. Typically, it means that the trajectory is pushed back by another inward jump, but in the other direction. As it will be discussed in the next section, the abrupt change of the direction is related to the negative or complex eigenvalues of matrix \mathbf{S} (9).

6 Control error estimation

6.1 Topological error estimate

The simplest estimation of the size of the absorbing sphere is based on the topological considerations, described in Section 5.1. According to the results presented there, the attractor that is farthest from the origin can be located at the m_{\max} th switching line (see (23)), at position y_{\max}^{SW} :

$$m_{\max} = \text{Int} \left(\frac{P}{P - \alpha^2} \right), \quad y_{\max}^{SW} = \frac{m_{\max}}{P}. \quad (35)$$

These results are valid if the diameters of the attractors are small compared to the distance of switching lines, i.e., no jumps or other escaping mechanisms occur. In this case

$$y_{\max}^{SW} \approx \frac{1}{P - \alpha^2} \quad (36)$$

provides a conservative estimate for the maximal control error.

6.2 General size estimate

6.2.1 Reformulation of the problem

Another – more general – estimation method is based on the fact that the micro-chaos map (10) can be rewritten to the following form:

$$\mathbf{y}_{j+1} = \mathbf{S}^j \mathbf{y}_0 - \sum_{k=0}^{j-1} \mathbf{S}^k \mathbf{b} \chi_k. \quad (37)$$

Unfortunately, matrix \mathbf{S} is typically a so-called non-normal matrix [13], i.e., its Euclidean norm (the greatest singular value) can be larger than 1, even if the eigenvalues are inside the unit circle. Still, in the latter case

$$\lim_{j \rightarrow \infty} \|\mathbf{S}^j\| = 0 \quad (38)$$

is fulfilled with any kind of norm [5]. Since the fractional numbers χ_k vary during the application of the micro-chaos map, the series (37) is divergent for almost all initial conditions. The only exceptions are the fixed points of the map.

However, there are cases when one can define a sequence $\tilde{\chi} \equiv \tilde{\chi}_0, \tilde{\chi}_1, \dots$ which is constant or can be divided into a finite number of constant subsequences such that (37) becomes convergent:

$$\mathbf{y}_{\infty}(\tilde{\chi}) \equiv - \lim_{j \rightarrow \infty} \sum_{k=0}^j \mathbf{S}^k \mathbf{b} \tilde{\chi}_k. \quad (39)$$

Our goal is to choose the sequence $\tilde{\chi}$ such that the maximal possible L^1 norm of the vector $\mathbf{y}_{\infty}(\tilde{\chi})$ provides an upper estimate for the size of the attracting domain at the origin.

$$|\mathbf{y}_{\infty \max}| \equiv \max_{\tilde{\chi}} |\mathbf{y}_{\infty}(\tilde{\chi})| \geq \max_{\tilde{\chi}} \limsup_{j \rightarrow \infty} |\mathbf{y}_j|. \quad (40)$$

The details of the application of this concept depend on the properties of the eigenvalues of matrix \mathbf{S} .

6.2.2 Eigenvalues of matrix \mathbf{S} – revisited

If the eigenvalues of \mathbf{S} are real, the number of sign changes in the characteristic equation (12) is equal to the number of positive eigenvalues, according to Descartes's sign rule. The coefficient of μ changes sign if the gain D assumes the value

$$D_1 = \frac{2c\gamma\alpha^2 + (e\gamma - c\gamma - \beta s)P}{\alpha^2 s}, \quad (41)$$

while the constant term changes sign at

$$D_0 = \frac{\gamma\alpha^2 + (ce\gamma - \gamma - \beta es)P}{\alpha^2 es}. \quad (42)$$

The eigenvalues $\mu_{1,2}$ are complex if the differential gain is between these two values:

$$D_c^{\pm} = \frac{\gamma(P - 2\alpha^2)(e - c) - P\beta s}{\alpha^2 s} \pm 2 \frac{\gamma\sqrt{(\alpha^2 - P)(-2ec + 1 + e^2)}}{\alpha s}. \quad (43)$$

We are interested in cases when the eigenvalues are inside the unit circle. It means that – since $D_c^+|_{P=\alpha^2} = D_c^-|_{P=\alpha^2}$ is fulfilled – D_c^- does not intersect the domain of stability. It can be shown after some algebra that

$$\begin{aligned} \mu_{1,2} \in \mathbb{C} & \quad \text{if } D_{b_1} < D < D_c^+, \\ \mu_{1,2} > 0 & \quad \text{if } D_c^+ < D < D_0, \\ \mu_1 > 0 \text{ and } \mu_2 < 0 & \quad \text{if } D_0 < D < D_{b_0}, \\ \mu_{1,2} < 0 & \quad \text{if } D_c^+ < D < D_0, \\ \mu_1 \mu_2 < 0 \text{ and } D < D_1 & \Rightarrow \mu_1 > |\mu_2|. \end{aligned} \quad (44)$$

The domains of various pairs of eigenvalues in the domain of stability are shown in Fig. 12. Topologically, the arrangement of these domains is invariant to the changes in the parameters: curve D_c^+ is tangent to D_{b_0} and D_{b_2} at the rightmost and lower left apexes of the triangular domain, respectively. D_0 is tangent to D_c^+ and D_1 passes through this tangent point and the upper left corner of the domain.

6.2.3 Possible estimates

In most of the cases, \mathbf{S} can be expressed as a diagonal matrix in the basis of eigenvectors. Let \mathbf{T} denote the corresponding (in general complex-valued) transformation matrix, while the eigenvalues of \mathbf{S} will be denoted by $\mu_{1,2}$. Using the notation $\mathbf{T}^{-1}\mathbf{b} = [\tilde{b}_1 \ \tilde{b}_2]^T$,

$$\begin{aligned} \mathbf{y}_{\infty}(\tilde{\chi}) &= -\mathbf{T} \sum_{k=0}^{\infty} \mathbf{T}^{-1} \mathbf{S}^k \mathbf{T} \mathbf{T}^{-1} \mathbf{b} \tilde{\chi}_k \\ &= -\mathbf{T} \sum_{k=0}^{\infty} \tilde{\chi}_k \begin{bmatrix} \lambda_1^k & 0 \\ 0 & \lambda_2^k \end{bmatrix} \begin{bmatrix} \tilde{b}_1 \\ \tilde{b}_2 \end{bmatrix}. \end{aligned} \quad (45)$$

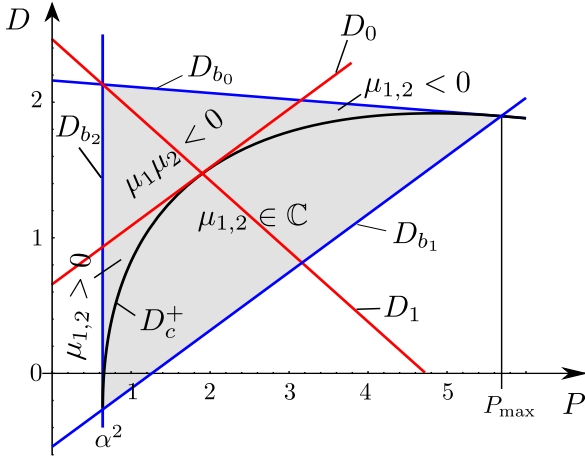


Fig. 12 The domain of asymptotic stability ($|\mu_{1,2}| < 1$) of the desired state $\mathbf{y} = \mathbf{0}$ without considering processing delay and quantization at $\alpha = 0.8$ and $\beta = 0.3$. The sub-domains of various pairs of eigenvalues are also shown.

- If the eigenvalues $\mu_{1,2}$ are positive real numbers, the maximal L^1 norm of \mathbf{y}_∞ can be obtained by the choice $\tilde{\chi}_k = 1, \forall k$, i.e.,

$$\mathbf{y}_{\infty \max} |_{\mu_{1,2} > 0} = \mathbf{T} \begin{bmatrix} \tilde{b}_1 \\ \frac{\mu_1 - 1}{\mu_2 - 1} \\ \frac{\tilde{b}_2}{\mu_2 - 1} \end{bmatrix}. \quad (46)$$

Moreover, it can be shown by substituting the expressions of \mathbf{S} and \mathbf{b} to (46) that – independently of the real or complex nature of the eigenvalues –

$$\mathbf{y}_\infty |_{\tilde{\chi}_k \equiv 1} = \begin{bmatrix} \frac{1}{P - \alpha^2} \\ 0 \end{bmatrix}, \quad (47)$$

just according to (36) that was derived on the basis of topological considerations!

- If both eigenvalues are negative, the choice $\tilde{\chi}_k = (-1)^k$ would provide the maximal L^1 norm in principle:

$$\mathbf{y}_{\infty \max} |_{\mu_{1,2} < 0} = \mathbf{T} \begin{bmatrix} -\tilde{b}_1 \\ \frac{\mu_1 + 1}{\mu_2 + 1} \\ -\frac{\tilde{b}_2}{\mu_2 + 1} \end{bmatrix}. \quad (48)$$

In practice, $\chi_k = (-1)^k$ means that the trajectory jumps between bands with alternating signs, e.g. from band $m = 1$ to band $m = -1$, then back.

- If $\mu_1 > 0$ and $\mu_2 < 0$, there are two different scenarios:

- 1) $\mu_1 > |\mu_2|$, i.e., the positive eigenvalue is dominant. In this case the estimate (46) can be used.
- 2) $\mu_1 < |\mu_2|$, i.e., the negative eigenvalue is dominant. In this case one can choose $\tilde{\chi}_k = (-1)^k$ for the negative eigenvalue and $\tilde{\chi}_k = 1$ for the positive one:

$$\mathbf{y}_{\infty \max} |_{\mu_1 \mu_2 < 0} = \mathbf{T} \begin{bmatrix} \tilde{b}_1 \\ \frac{\mu_1 - 1}{\mu_2 + 1} \\ -\frac{\tilde{b}_2}{\mu_2 + 1} \end{bmatrix}. \quad (49)$$

- If the eigenvalues form a complex conjugate pair, the error estimation can be performed as follows. Let ρ and ϕ denote the modulus and the argument of μ_1 , respectively. With this notation,

$$\begin{aligned} & \mathbf{T} \begin{bmatrix} \sum_{k=0}^{\infty} \mu_1^k \tilde{\chi}_k \tilde{b}_1 \\ \sum_{k=0}^{\infty} \mu_2^k \tilde{\chi}_k \tilde{b}_2 \end{bmatrix} = \\ & = \mathbf{T} \begin{bmatrix} \sum_{k=0}^{\infty} \rho^k (\cos(k\phi) + i \sin(k\phi)) \tilde{\chi}_k \tilde{b}_1 \\ \sum_{k=0}^{\infty} \rho^k (\cos(k\phi) - i \sin(k\phi)) \tilde{\chi}_k \tilde{b}_2 \end{bmatrix} = \\ & = \mathbf{T} \sum_{k=0}^{\infty} \rho^k \cos(k\phi) \tilde{\chi}_k \begin{bmatrix} \tilde{b}_1 \\ \tilde{b}_2 \end{bmatrix} + \quad (50) \\ & + i \mathbf{T} \sum_{k=0}^{\infty} \rho^k \sin(k\phi) \tilde{\chi}_k \begin{bmatrix} \tilde{b}_1 \\ -\tilde{b}_2 \end{bmatrix} = \\ & = \sum_{k=0}^{\infty} \rho^k \cos(k\phi) \tilde{\chi}_k \mathbf{b} + \sum_{k=0}^{\infty} \rho^k \sin(k\phi) \tilde{\chi}_k \mathbf{b}^-, \end{aligned}$$

where $\mathbf{b}^- = i \mathbf{T} [\tilde{b}_1 \quad -\tilde{b}_2]^T$ is a real valued vector. Consequently, \mathbf{y}_∞ can be expressed by the elements of \mathbf{b} and \mathbf{b}^- in the form

$$\mathbf{y}_\infty = \begin{bmatrix} \sum_{k=0}^{\infty} \rho^k \tilde{\chi}_k A_1 \sin(k\phi + \varepsilon_1) \\ \sum_{k=0}^{\infty} \rho^k \tilde{\chi}_k A_2 \sin(k\phi + \varepsilon_2) \end{bmatrix}. \quad (51)$$

It is clearly seen that the maximal displacement can be estimated by the choice $\tilde{\chi}_k = \text{sign}(\sin(k\phi + \varepsilon_1))$, while the maximal velocity is obtained with $\tilde{\chi}_k = \text{sign}(\sin(k\phi + \varepsilon_2))$. Since we did not find an analytical formula for the calculation of these series, truncated series can be used in practice. If the series are truncated at $k = n - 1$, the residual can be overestimated as

$$\epsilon_i \equiv \sum_{k=n}^{\infty} \rho^k A_i = \frac{A_i \rho^n}{1 - \rho}, \quad i = 1, 2. \quad (52)$$

Thus, the necessary number of members in the series can be estimated as

$$n > \frac{\log((1 - \rho)\epsilon_i) - \log(A_i)}{\log(\rho)}, \quad i = 1, 2. \quad (53)$$

- In the rare special case, when \mathbf{S} is not diagonalizable, it still can be transformed to Jordan form. In this case,

$$\mathbf{y}_\infty = -\mathbf{T} \sum_{k=0}^{\infty} \tilde{\chi}_k \begin{bmatrix} \mu_1^k + \tilde{b}_1 \\ \mu_2^k \tilde{b}_2 \end{bmatrix}, \quad (54)$$

which cannot be made convergent with a constant sequence $\tilde{\chi}_k$. Actually, further results could be used from the theory of non-normal matrices [13] for the estimation of the control error. Unfortunately the upper estimates that are based on the general theory usually provide unrealistically large (but finite) numbers. These large numbers cannot be used for the prediction of the behaviour of the real control system.

To check our results, we performed a long series of numerical simulations at several parameters, where P and D assumed values in the corresponding domain of stability. Since the damping parameter β decreases the lengths of jumps – and the size of the absorbing sphere – we focused on the worst case scenario, i.e., $\beta = 0$. As Fig. 13 shows, the simple topological estimate (47) can be used even in a large subset of complex eigenvalues if the instability parameter α is small. Moreover, the prediction of the phase-space structure based on the crisis phenomenon is also reliable in broad parameter domains. As α is increased, the domains, where both the structure prediction and the size prediction fail, increase. Besides the domain of complex eigenvalues (\mathbb{C}) and the domain of negative eigenvalues (\mathbb{R}^{--}), the predictions may fail in the \mathbb{R}^{-+} domain, too, where the negative eigenvalue has larger modulus. Similarly, \mathbb{R}^{+-} denotes the domain where the positive eigenvalue is dominant, and there are only positive eigenvalues in \mathbb{R}^{++} . The topological estimate was found to be always reliable in these two domains.

Figs. 14 and 15 show the largest possible displacement coordinate that was estimated by numerical simulation and Eqs. (46), (48) (49) and (51), taking into account the absolute value of the first component of \mathbf{y}_∞ . As it can be seen, the proposed method is fairly accurate or slightly overestimates the maximal displacement coordinate in the domain \mathbb{R}^{+-} and even in \mathbb{R}^{++} . As a consequence of the border collisions of the fixed points up to $P = 2\alpha^2 = 1.28$, clearly distinguishable steps appear in the simulation results depicted in Fig. 14. A small deviance occurs in \mathbb{R}^{--} . Here Eq. (48) slightly underestimates the maximal displacement in some parts of the domain. Note that the estimate is based on the maximal L^1 norm of \mathbf{y}_∞ , while the maximal displacement coordinate is shown in Fig. 14. The worst – but still conservative – error estimate is obtained in the domain \mathbb{C} . The step in the simulation results at $P = 4.34$ is related to the possibility of inward jumps from $m = 1$ to $m = -1$.

Fig. 15 was drawn at parameters $\alpha = 0.1$, $\beta = 0$ and $D = 1$. There is only a single true fixed point if $P > 0.02$, thus, no steps can be observed in the simulation results on the left hand side of the figure. However, non-monotonous steps occur at large values of P that are related to border collisions of higher-order periodic orbits. Similar results were obtained in broad parameter domains. It is worth to mention that a secondary digital effect occurred at small values of α ($\alpha < 0.01$): during the simulation of the micro-chaos map certain trajectories could escape from attractors far from the origin. This phenomenon is clearly related to the finite number of digits used during the simulation [14].

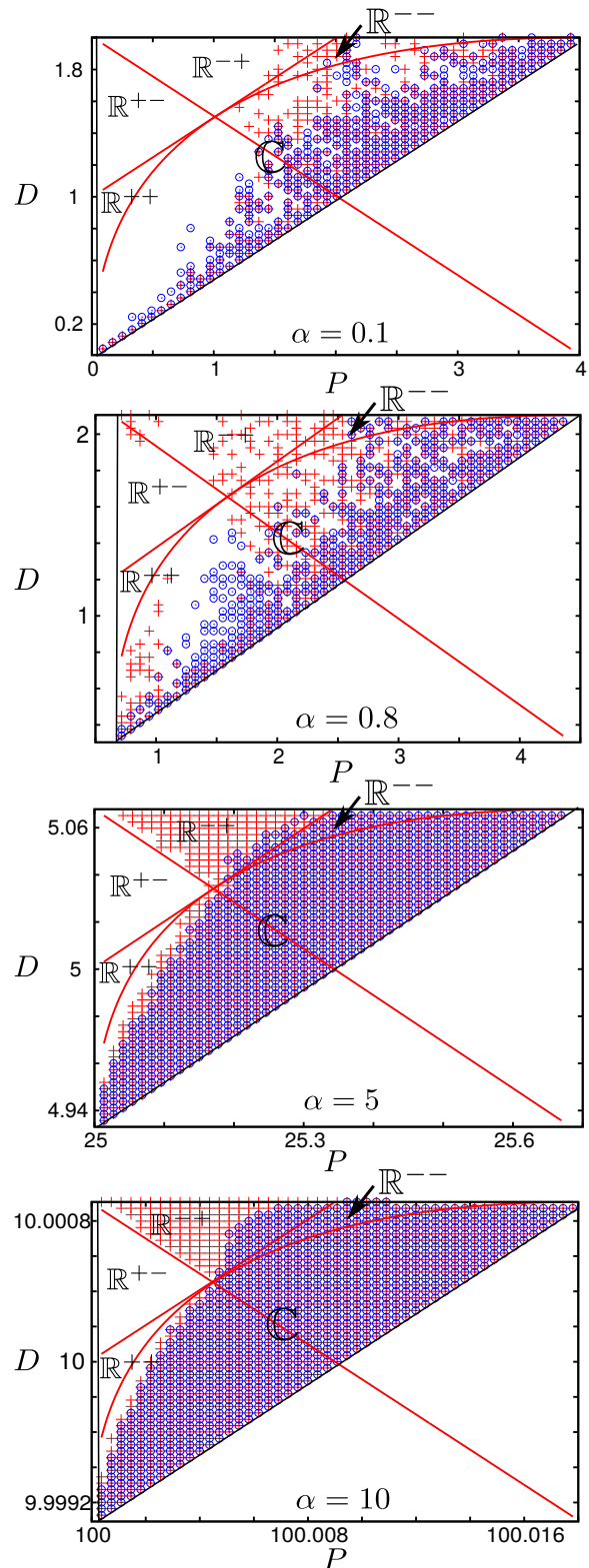


Fig. 13 The estimated control error at parameters $\beta = 0$ and $\alpha = 0.1$, $\alpha = 0.8$, $\alpha = 5$ and $\alpha = 10$. Plus signs indicate parameter values where the crisis-based prediction failed. Circles show cases where the simple estimate $y_{\max} = 1/(P - \alpha^2)$ failed.

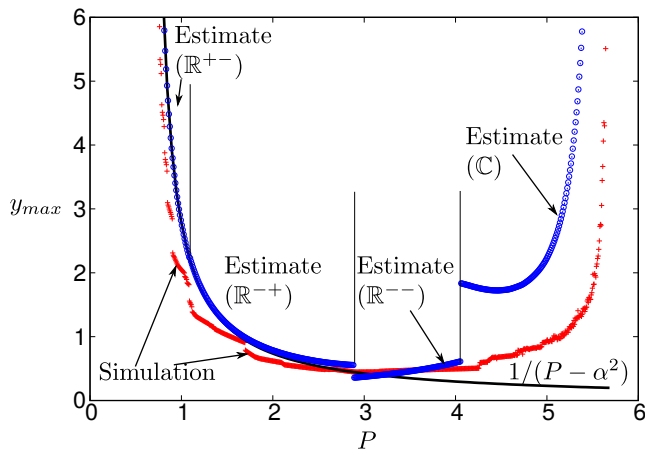


Fig. 14 The estimated control error in terms of maximal displacement at parameters $D \equiv D(P_{\max}) = 1.89749$, $\alpha = 0.8$, $\beta = 0.3$. Topological estimate: $y_{\max} = 1/(P - \alpha^2)$.

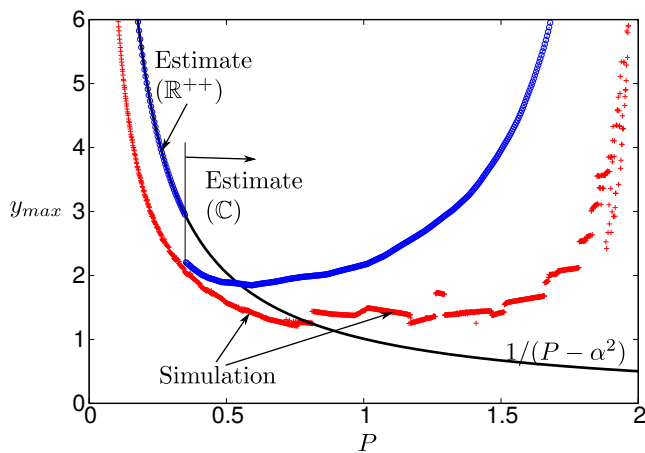


Fig. 15 The estimated control error in terms of maximal displacement at parameters $D = 1$, $\alpha = 0.1$, $\beta = 0$. Topological estimate: $y_{\max} = 1/(P - \alpha^2)$.

7 Conclusions

The main goal of this contribution was the exploration of phase-space structures in a simple PD-controlled oscillator where chaotic oscillations occur due to sampling and quantization. The results may help to provide reliable conservative estimates of the control error, i.e., the maximal distance from the origin. We found that several fixed points can coexist in the phase-space. Their number is independent of gain D and viscous damping β , but increases with gain P and decreases with instability parameter α via border collision bifurcations. Certainly, if P and D are restricted to the domain of stability, the number of fixed points is bounded from below and the bound depends also on β .

It can be shown that strange repellers or attractors are formed between each pair of fixed points. Conditions

of crisis bifurcations were derived that can be used for the determination of repelling and attracting properties of the strange sets. At large values of parameter α trajectories can jump farther away from the origin, while at large values of P the trajectories typically jump towards the origin. In the latter case, certain trajectories may even jump over the origin, leading to rather large control error. The increase of parameter β helps to decrease the length of possible jumps. In a counter-intuitive way, larger jumps may occur if parameter D is increased. This phenomenon is related to the fact that the slope of the switching lines decreases with D .

There are several possible bifurcations that were not examined in the present paper but still can influence the control error. Because of the complexity of the phase-space, these bifurcations cannot be fully explored. This is why we derived a set of analytical estimates for five different cases, depending on the eigenvalues of the matrix \mathbf{S} . Even a simple formula $y_{\max} = 1/(P - \alpha^2)$ was derived that is valid if the positive eigenvalue of matrix \mathbf{S} is dominant. The analytical results were checked by numerical simulation on a digital computer, which had to be performed carefully due to a secondary digital effect.

Acknowledgements This research was supported by the Hungarian National Science Foundation under grant no. OTKA K 83890.

References

1. Kuo, B.C.: Digital Control Systems. SRL Publishing, Champaign, IL, USA (1977)
2. Delchamps, F.D.: Stabilizing a linear system with quantized state feedback. IEEE Trans. Autom. Contr., 35, 916-924 (1990)
3. Chen, G., Dong, X.: From Chaos to Order: Methodologies, Perspectives and Applications. World Scientific, Singapore (1998)
4. Haller, G., Stépán, G.: Micro-Chaos in Digital Control. J. Nonlinear Sci. 6, 415-448 (1996)
5. Csernák, G., Stépán, G.: Digital Control as Source of Chaotic Behavior. Int. J. Bifurcat. Chaos, 20(5), 1365-1378 (2010)
6. Widrow, B., Kollár, I.: Quantization Noise: Roundoff Error in Digital Computation. Signal Processing, Control, and Communications. Cambridge University Press, Cambridge, UK, 778 p. (2008)
7. Csernák, G., Gyebroszki, G., Stépán, G.: Multi-baker Map as a Model of Digital PD Control. Int. J. Bifurcat. Chaos, 26(2) (2016) Accepted on Sep 05, 2015, scheduled for publication in the February issue of 2016.
8. Milton, J.G., Bélair, J.: Chaos, Noise and Extinction in Models of Population Growth. Theor. Popul. Biol., 37(2) (1990)
9. Cabrera, J.L., Milton, J.G.: Stick balancing: On-off intermittency and survival times. Nonlinear Studies, 11(3), 305-317 (2004)

10. Lakshmikantham, V., Leela, S., Martynyuk, A.A.: Practical Stability of Nonlinear Systems. World Scientific, Singapore (1990)
11. Insperger, T., Milton, J., Stépán, G.: Semidiscretization for Time-Delayed Neural Balance Control. *SIAM J. Appl. Dyn. Syst.*, 14(3), 12581277 (2015)
12. Csernák, G., Stépán, G.: Quick Estimation of Escape Rate with the Help of Fractal Dimension, *Communications in Nonlinear Science and Numerical Simulation*, 11(5), 595-605 (2005)
13. Trefethen, L. N., Embree, M.: Spectra And Pseudospectra: The Behavior of Nonnormal Matrices And Operators. Princeton University Press (2005)
14. Domokos, G., Szász, D.: Ulam's Scheme Revisited: Digital Modeling of Chaotic Attractors Via Micro-Perturbations. *Discret. Contin. Dyn. S., Series A.* 9(4), 859-876 (2003)